Journal of Colloid and Interface Science 462 (2016) 191–199

Contents lists available at ScienceDirect

Journal of Colloid and Interface Science

journal homepage: www.elsevier.com/locate/jcis

In situ hydrothermal synthesis of a novel hierarchically porous TS-1/modified-diatomite composite for methylene blue (MB) removal by the synergistic effect of adsorption and photocatalysis

Weiwei Yuan [a,b,c], Peng Yuan [a,c,*], Dong Liu [a,c], Wenbin Yu [a,b,c], Minwang Laipan [a,b,c], Liangliang Deng [a,b,c], Fanrong Chen [a,c]

[a] CAS Key Laboratory of Mineralogy and Metallogeny, Guangzhou Institute of Geochemistry, Chinese Academy of Sciences, Wushan, Guangzhou 510640, China
[b] University of Chinese Academy of Sciences, Beijing 100039, China
[c] Guangdong Provincial Key Laboratory of Mineral Physics and Materials, Wushan, Guangzhou 510640, China

GRAPHICAL ABSTRACT

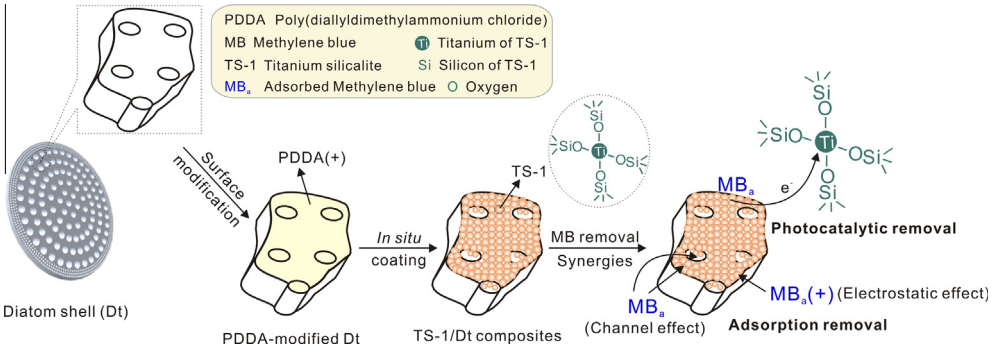

ARTICLE INFO

Article history:
Received 3 September 2015
Revised 28 September 2015
Accepted 29 September 2015
Available online 22 October 2015

Keywords:
Hierarchically porous structure
TS-1/modified-diatomite composite
In situ hydrothermal method
Synergistic effect
Methylene blue

ABSTRACT

Hierarchically porous TS-1/modified-diatomite composites with high removal efficiency for methylene blue (MB) were prepared via a facile *in situ* hydrothermal route. The surface charge state of the diatomite was modified to enhance the electrostatic interactions, followed by *in situ* hydrothermal coating with TS-1 nanoparticles. The zeolite loading amount in the composites could be adjusted by changing the hydrothermal time. The highest specific surface area and micropore volume of the obtained composites were 521.3 m^2/g and 0.254 cm^3/g, respectively, with an optimized zeolite loading amount of 96.8%. Based on the synergistic effect of efficient adsorption and photocatalysis resulting from the newly formed hierarchically porous structure and improved dispersion of TS-1 nanoparticles onto diatomite, the composites' removal efficiency for MB reached 99.1% after 2 h of photocatalytic reaction, even higher than that observed using pure TS-1 nanoparticles. Moreover, the superior MB removal kinetics of the composites were well represented by a pseudo-first-order model, with a rate constant (5.28×10^{-2} min^{-1}) more than twice as high as that of pure TS-1 nanoparticles (2.43×10^{-2} min^{-1}). The significant dye removal performance of this novel TS-1/modified-diatomite composite indicates that it is a promising candidate for use in waste water treatment.

* Corresponding author at: Guangzhou Institute of Geochemistry, Chinese Academy of Sciences, Wushan, Guangzhou 510640, China.
E-mail address: yuanpeng@gig.ac.cn (P. Yuan).

http://dx.doi.org/10.1016/j.jcis.2015.09.067
0021-9797/

1. Introduction

Dye effluents from sources such as the textile, dyestuff manufacturing and printing industries have become increasingly important over the last decades because of their environmental hazards. Most dyes are toxic, and some are even carcinogenic and mutagenic to humans and animals [1–3]. For the remediation of waste water containing dyes, physical, chemical and biological methods have been extensively used, including adsorption, filtration and membrane separation [4–6], electrochemical destruction [7] and advanced oxidation technology [8]. Among these methods, heterogeneous photocatalytic oxidation is considered to be the most common and promising process for the removal of dye effluents because of its high removal efficiency, environmental protection property and simplicity of use [9–11]. The removal of dye organic molecules occurs through hydroxyl radical oxidation when a semiconductor catalyst is activated by light.

Recently, titanium silicalite (abbreviated as TS-1 hereafter), especially TS-1 nanoparticles, has been developed as a semiconductor catalyst for heterogeneous photocatalytic reactions [12–14]. As a novel molecular sieve material that was first synthesized by Taramasso and coworkers in 1983 [15], TS-1 is a derivative of silicalite-1 zeolite and is formed when titanium atoms are introduced into lattice positions of the silicalite-1 framework. Compared to conventional TiO_2 catalysts, TS-1 nanoparticles exhibit significant adsorption capacity because of their abundant microporous structures and high specific surface areas. Moreover, the intrinsic activity per Ti atom in TS-1 is higher than that in TiO_2. The higher adsorption capacity and Ti-utilization efficiency enable TS-1 to facilitate both physical adsorption and chemical oxidation [13], making it a better choice for the removal of dye effluents than conventional TiO_2 nanoparticles, which exhibit only a single chemical action.

In photocatalytic reactions of TS-1 nanoparticles, Ti species are modified via the adsorption of organic molecules, followed by charge transfer under UV irradiation ($Ti^{4+} + O^{2-} \rightarrow Ti^{3+} + O^{-}$) [16–18]. Therefore, increasing the contact area between TS-1 nanoparticles and organic molecules is critical to improve removal efficiency [16]. However, the agglomeration of nanoparticles is known to lower their effective surface area [19,20] and reduce their contact with dyes. Loading methods in which TS-1 nanoparticles are coated with organic or inorganic supports represent an alternative strategy to overcome the agglomeration of nanoparticles. Non-porous supports, such as glass [21,22] and polydimethylsiloxane (PDMS) [23,24], have been used as coating matrices for TS-1 nanoparticles; however, the resulting composites formed from TS-1 nanoparticles and non-porous supports exhibit monomodal microporosity. Pores in TS-1 are smaller than 1 nm and are inaccessible for some organic macromolecules [25–27]. Thus, the structural micropores of TS-1 limit the adsorption and diffusion of most dyes, which adversely affects subsequent photocatalysis. Currently, substantial efforts have been made to identify appropriate macroporous supports for fabricating hierarchically porous TS-1 composites, improving the dispersity and stability of TS-1 nanoparticles, while simultaneously developing their catalytic compatibility for various organic molecules. Au et al. [28] used porous stainless steel as a support. In their experiments, silicalite-1 seed crystals were assembled on the surface of porous stainless steel, and a secondary growth process then introduced Ti atoms into the silicalite-1 framework. Wang et al. [29] and Wang et al. [30] also reported the synthesis of TS-1/porous α-alumina composites using the pre-seeding and regrowth technique. The TS-1 product possessed hierarchically porous structures, comprising macropores from the supports and micropores from TS-1 nanoparticles, which should lead to excellent catalytic performance with organic molecules. However, both the porous stainless steel and α-alumina supports were synthesized and required complicated pretreatments for the coating process, potentially increasing the preparation costs. In addition, the pre-seeding and regrowth technique required a long synthesis period, which would limit the practical application of the resulting composites for catalysis. Consequently, identifying porous supports with economical viability and facile preparation methods with practical feasibility are very important for improving the catalytic efficiency of TS-1 nanoparticles.

Diatomite is a potential candidate for the preparation of hierarchically porous composites [20,31–37] because it occurs naturally with well-developed porosity. Diatomite, which is also known as diatomaceous earth or kieselgur, is a fossil assemblage of diatom shells consisting of amorphous hydrated silica ($SiO_2 \cdot nH_2O$) and classified as opal-A in mineralogy. It is characterized by a macroporous structure, with pore sizes ranging from nanometers to micrometers [38–40]. As a fine-grained, low-density biogenetic sediment that is non-toxic and readily available in ton quantities at low cost, diatomite has been studied to evaluate its feasibility as a support for TS-1 nanoparticle coating. Liu et al. [32] and Liu et al. [41–43] proposed a mechanical mixing method for the preparation of TS-1/diatomite. They found that the TS-1/diatomite catalyst exhibited good performance for the hydroxylation of toluene and phenol respectively. Nonetheless, this mechanical mixing resulted in inhomogeneous coating, leading to a relatively low Brunauer–Emmett–Teller (BET) surface area (222.5 m^2/g) and micropore volume (0.05 cm^3/g), indicating that the problem of TS-1 nanoparticles agglomeration remained largely unresolved.

Previous studies have shown that diatomite and TS-1 nanoparticles are both negatively charged in alkaline solutions, with similar isoelectric points of ca. 2.0 [44] and ca. 3.0 [45], respectively; this means that their loading relationship is greatly influenced by electrostatic repulsion. Therefore, to improve the loading relationship and mitigate the agglomeration of TS-1 nanoparticles, modifying the surface charge of diatomite is a promising route. To the best of our knowledge, such studies have not yet been reported.

In the present study, a novel TS-1/modified-diatomite composite with a hierarchically porous structure and high dispersity was synthesized via a facile *in situ* hydrothermal method based on the surface charge modification of diatomite (forming the pre-modified diatomite). Methylene blue (MB), a typical macromolecular dye with a rectangular volume and dimensions of $17.0 \times 7.6 \times 3.25$ Å^3 [46], was used as the model of organic dye molecule [47–48] to evaluate the performance of the TS-1/modified-diatomite composites. Moreover, the structural diversity of the composites synthesized under various crystallization times and its influence on MB removal are also discussed.

2. Experimental

2.1. Reagents and materials

Tetraethoxysilane (TEOS, 99%) and poly(diallyldimethylammonium chloride) (PDDA, 20% aqueous solution) were purchased from Aldrich. Tetrabutylorthotitanate (TBOT) was supplied by Shanghai Lingfeng Chemical Co., Ltd. Tetrapropylammonium hydroxide (TPAOH, 25% aqueous solution) was obtained from Zhejiang Kente Chemical Co., Ltd. Isopropanol was supplied by Sinopharm Chemical Reagent Co., Ltd. MB ($C_{16}H_{18}ClN_3S \cdot 3H_2O$) of reagent-grade purity (⩾98.5%) was purchased from Tianjin Tianxin Fine Chemical Industry Development Center. Distilled water (18.2 ΩM cm) was used in all of the experiments. Raw diatomite (Dt) was obtained from the Changbai deposit in the province of Jilin, China. Its chemical composition (wt%) was as follows: SiO_2, 86.18; Al_2O_3, 3.08;

Fe_2O_3, 1.47; MgO, 0.33; CaO, 0.37; Na_2O, 0.05; K_2O, 0.51; MnO, 0.01; P_2O_5, 0.06; TiO_2, 0.17; and loss on ignition, 8.56. All of the reagents and materials were used as received.

2.2. In situ hydrothermal synthesis of TS-1/modified-diatomite composites

A TS-1 precursor suspension with a TEOS:TBOT:TPAOH:isopropanol:H_2O molar ratio of 1:0.03:0.32:0.77:18 was prepared [22]. To do this, 10.64 ml of TPAOH (25% aqueous solution) was added slowly to 12.85 ml of TEOS, and the suspension was continuously stirred and aged for 24 h at room temperature to fully hydrolyze the silicon source. Then, a mixed solution of 0.59 ml of TBOT and 3.39 ml of isopropanol was added dropwise under vigorous stirring until the initially white solution became clear. Finally, another 3.91 ml of TPAOH was added slowly. The resulting mixture was heated at 353 K for 1 h to remove the isopropanol. The viscous mixture was added to 18.7 ml of distilled water, and the obtained suspension (pH = 12.4) was transferred to a sealed Teflon-lined stainless steel autoclave.

1.5 g of Dt was submerged into 80 ml of 0.5% PDDA solution for 2 h to form a PDDA-modified diatomite, which was dried and mixed with the TS-1 precursor suspension subsequently. The autoclave was then placed in an oven and heated at 443 K for 3, 12, and 24 h to facilitate crystallization. Subsequently, the as-synthesized sample was centrifuged, washed thoroughly and calcined at 823 K for 6 h to remove the organic template. The resulting samples (TS-1/Dt composite) were denoted as TS-1/Dt_3, TS-1/Dt_{12}, and TS-1/Dt_{24}, respectively. Pure TS-1 nanoparticles with crystallization times of 12 h and 24 h were denoted as TS-1_{12} and TS-1_{24}, respectively.

2.3. Characterization methods

X-ray diffraction (XRD) patterns were recorded on a Bruker D8 Advance diffractometer with a Ni filter and a Cu Kα radiation source (λ = 0.154 nm) operated under a generating voltage of 40 kV and a current of 40 mA. The diffractometer was at a scan rate of 3° (2θ)/min. Scanning electron microscopy (SEM) images were obtained using a ZEISS Supra 55 field emission scanning electron microscope.

X-ray photoelectron spectroscopy (XPS) measurement was performed using a Thermo Fisher Scientific K-Alpha instrument equipped with a monochromatic Al Ka X-ray source (excitation energy = 1468.6 eV). Prior to measurement, the spectrometer analyzer chamber was vacuumized to 5×10^{-8} mbar or lower. The testing spot size was set to 400 μm and pass energy 100 eV for wide scanning, 30 eV for narrow scanning. In charge-up correction, the spectrum line of C 1s = 284.8 eV was employed. Spectrum fitting was carried out using the XPS Peakfit software with the Smart background correction.

Mercury intrusion tests to evaluate the macropore size distribution of the samples were conducted on a Micromeritics AutoPore IV 9500 porosimeter in the pressure range from 0.1 to 60,000 psi. A Micromeritics ASAP 2020 system was used to measure nitrogen adsorption–desorption isotherms at liquid nitrogen temperature (77 K). All of the samples were degassed at 573 K under vacuum for 12 h before measurement. The specific area (S_{BET}) was calculated from the nitrogen adsorption data on the basis of the multi-point Brunauer–Emmett–Teller (BET) equation. The Micropore surface area ($S_{micropore}$) of the composites was derived from t-plot method. Micropore and mesopore size distributions in the range from 0 to 20 nm were determined using the non-local density functional theory (NLDFT) model.

2.4. Photocatalytic reaction

The batch photoreactor used in this work was purchased from Shanghai Bilon Instruments Co., Ltd. The removal efficiencies of the resulting composites were evaluated in the photocatalysis of MB using ultraviolet (UV) irradiation from a 300 W HP Hg lamp (λ_{max} = 365 nm). In a typical reaction, 0.05 g of TS-1/Dt composite and 50 ml of MB solution with an initial concentration of 28.65 mg L^{-1} (pH = 8.02) were mixed in a quartz reactor, placed on a magnetic stirrer, and irradiated under UV for 2 h with vigorous stirring. Aliquots (0.5 ml) of supernatant were collected every 10 or 20 min and diluted and filtrated using a 0.45 μm filter membrane. The remaining MB concentration was monitored by UV–vis spectroscopy (model 759S, Shanghai Jinghua Instruments Co., Ltd.) at a maximum absorption wavelength of 664 nm. The adsorption of MB on the TS-1/Dt composites was also conducted on the magnetic stirrer in darkness for 3 h.

3. Results and discussion

3.1. Textural and morphological characterization of the composites

XRD patterns of Dt, TS-1_{24} and TS-1/Dt composites are shown in Fig. 1. The XRD pattern of Dt is that of amorphous Opal-A, with a broad peak centered at approximately 21.8°(2θ), corresponding to a *d*-spacing of 0.409 nm [39]. The (101) reflection peak at 26.6°(2θ) indicates the presence of a small amount of quartz

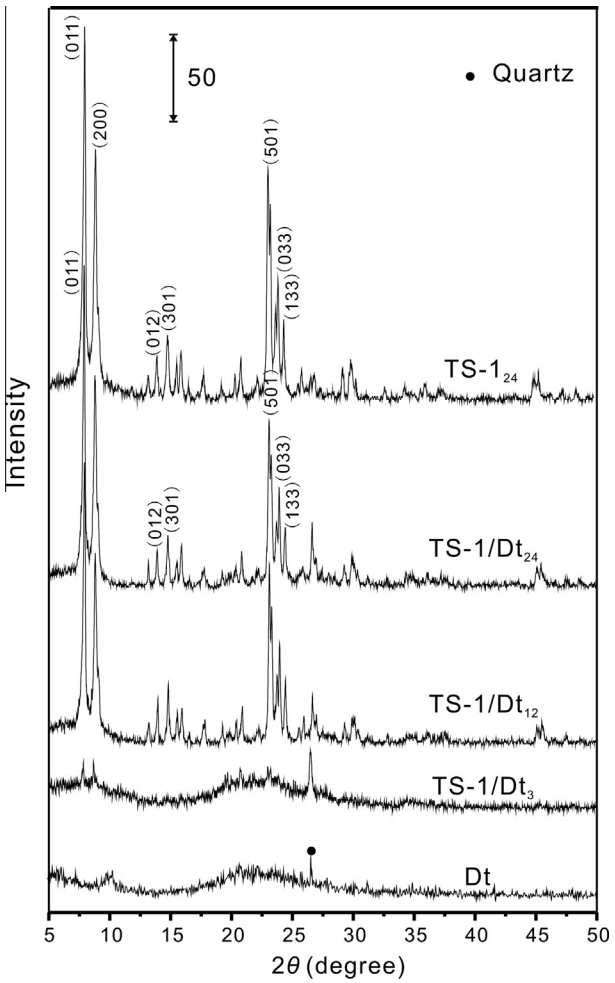

Fig. 1. XRD patterns of Dt, TS-1_{24} and TS-1/Dt composites.

impurity in Dt. TS-1_{24} exhibited typical peaks at 7.8°, 8.8°, 23°, 23.6°, and 24.4° (2θ), corresponding to the characteristic reflections of MIF-type zeolite, (011), (200), (501), (033), and (133), respectively. Moreover, two peak splittings, caused by the conversion from monoclinic silicalite-1 to the orthorhombic structure, appeared at $2\theta = 24.4°$ and 29.5° in TS-1_{24}, suggesting that titanium atoms were introduced into the silicalite-1 framework, and thus, TS-1 was synthesized. The XRD pattern of TS-1/Dt_3 displayed peaks of both TS-1 zeolite and amorphous opal-A, indicating the coating of TS-1 nanoparticles on the surface of the diatomite. The intensities of diffraction peaks for the MFI-type zeolite are stronger in TS-1/Dt_{24} than in TS-1/Dt_3 and TS-1/Dt_{12}, indicating that a longer *in situ* hydrothermal time results in higher crystallinity of the TS-1 nanoparticles. In contrast to earlier works, in which anatase and/or extra-framework Ti were normally present for a Ti content in TS-1 exceeding 2.5 at.% [49], no additional TiO_2 crystalline phases, such as anatase ($2\theta = 25.5°$), were detected, even at 3.0 at.% Ti. This phenomenon can be ascribed to the short hydrothermal time, which prevents the crystallization of amorphous TiO_2 gel produced during the hydrolysis of the titanium source.

As shown in the SEM images (Fig. 2a), the dominant diatom of Dt, classified as *Coscinodiscus* Ehrenberg (*Centrales*), is disc-shaped and has highly developed macropores with regular pore diameters (0.1–0.8 μm) varying from the edge of the disc to the center [39]. The macroporous structure and smooth surface of the diatom shell were clearly observed at high magnification (Fig. 2a). SEM images of TS-1/Dt_3 (Fig. 2b) showed that the disc-shaped morphology of diatomite remained intact after hydrothermal treatment for 3 h. Observed under high magnification, the smooth surface of the diatom shell appeared uneven due to a small amount of spherical TS-1 nanoparticles with an average particle size of ca. 200 nm. The macroporous structure of the diatom shell was preserved, indicating that the obtained TS-1/Dt composites possessed hierarchical pores: macropores from diatomite and micropores from TS-1. SEM images of TS-1/Dt_{12} (Fig. 2c) showed that the diatomite surface was primarily coated with TS-1 nanoparticles (200 nm). The macropore size reduction in the diatomite support was caused by the partial obstruction by TS-1 nanoparticles. Moreover, some spherical TS-1 nanoparticles developed into larger hexagonal prisms (Fig. 2c). This indicates that the crystallinity of the TS-1 nanoparticles increased gradually with increasing crystallization time, which agrees with the XRD results (Fig. 1). For TS-1/Dt_{24}, the diatomite surface was completely covered by TS-1 nanoparticles, and several TS-1 nanoparticles on the surface of the diatomite tended to fuse into flakes, as shown in Fig. 2d. In the diatomite support, some of the macropores could still be identified (Fig. 2d), verifying the hierarchically porous structure of TS-1/Dt_{24}.

Si 2p, O 1s, Ti 2p and C 1s XPS spectra were measured for each sample. The binding energies of Si 2p and O 1s, shown in Supplementary Table S1, were 103.7 ± 0.1 eV and 532.9 ± 0.3 eV, respectively. The slight shift to lower binding energy in TS-1/Dt_3 (103.0 eV) was attributed to the lower loading amounts and crystallinity of the TS-1 nanoparticles [49]. The deconvolution of the Ti 2p spectrum from the surface of each sample is shown in Fig. 3. In general, the existing state of Ti reflected by the XPS spectra is classified as follows: (i) Ti^{4+} in a tetrahedral position in the silicalite framework, indicated by the Ti $2p_{3/2}$ peak maximum at 460.0 eV [49]; (ii) extra-framework hydrated Ti^{4+} confirmed by the presence of the Ti $2p_{3/2}$ peak maximum at 458.6 eV [50,51]; and (iii) a small fraction of octahedrally coordinated Ti^{4+} in a separate phase, indicated by the Ti $2p_{3/2}$ peak maximum at a lower binding energy [50,51]. The Ti 2p XPS of TS-1/Dt_3 (Fig. 3a) exhibited two peaks centered at 459.7 and 465.5 eV, which were assigned to Ti $2p_{3/2}$ and the corresponding Ti $2p_{1/2}$, respectively. These peaks are typically ascribed to tetrahedral Ti^{4+} in the silicalite framework, verifying the synthesis of TS-1 nanoparticles on the diatomite surface. Ti 2p XPS of TS-1/Dt_{12} (Fig. 3b) was deconvoluted into two Ti $2p_{3/2}$ peaks centered at 460.0 and 458.8 eV and two Ti $2p_{1/2}$ peaks at 465.5 and 464.3 eV, which were assigned to Ti^{4+} in the TS-1 framework and hydrated Ti^{4+} in species, respectively. The additional appearance of Ti $2p_{3/2}$ peaks at 458.8 eV in TS-1/Dt_{12} compared to TS-1/Dt_3 can be explained by the presence of negatively amorphous hydrated TiO_2 gels [52]. These gels were produced via the complete hydrolysis of tetrabutylorthotitanate and were adsorbed onto the PDDA-modified diatomite, demonstrating the benign adsorption abilities of the modified support. TS-1/Dt_{24} (Fig. 3c) had characteristics similar to TS-1/Dt_{12}, with Ti $2p_{3/2}$ peaks centered at 460.2 and 458.8 eV ascribed to Ti^{4+} in the TS-1 framework and hydrated Ti^{4+}, respectively. However, the slight shift of the binding energy from 459.7 to 460.0 and 460.2 eV suggests that the loading amount of TS-1 nanoparticles on the surface of the diatomite was the greatest on TS-1/Dt_{24} and the least on TS-1/Dt_3, in accordance with the SEM results in Fig. 2. TS-1_{24} (Fig. 3d) displayed two Ti $2p_{3/2}$ peaks at 460.3 and 458.2 eV and two Ti $2p_{1/2}$ peaks at 465.9 and 464.0 eV, which were attributed to tetrahedral Ti^{4+} in the TS-1 framework and a small fraction of octahedrally coordinated Ti^{4+}, respectively. The presence of the latter in TS-1_{24} was due to the presence of oxygen atoms, which resulted from a small amount of surrounding TiO_2, donating electrons from unshared electron pairs.

As shown in Fig. 4, the N_2 adsorption–desorption isotherm of Dt is of type II with a minor H3 hysteresis loop, according to IUPAC classification, which indicates the existence of abundant macropores and some mesopores, consistent with results from our previous study [20]. The sharp increase in the N_2 adsorption at relatively high pressures also signifies the existence of macropores in diatomite. For TS-1/Dt_3, the steep increase in adsorption followed by a mild stage at relatively low pressures ($P/P_0 \leqslant 0.1$) indicates the filling of the TS-1 micropores, and the H3 hysteresis loop of the isotherm is associated with the filling and emptying of the mesopores. These mesopores should be a result of the stacking of TS-1 nanoparticles. The steadily increasing N_2 adsorption amount of TS-1/Dt_3 as P/P_0 approached 1.0 is ascribed to the adsorption on the external surface of TS-1 nanoparticles, and the adsorption in the macropores of the diatomite. For TS-1/Dt_{12} and TS-1/Dt_{24}, the higher N_2 adsorption amount at relatively low pressures ($P/P_0 \leqslant 0.1$) compared with TS-1/Dt_3 indicates the emergence of more micropores, consistent with their higher zeolite loading amounts, as revealed by SEM in Fig. 2c and d. TS-1/Dt_{24} and TS-1_{24} demonstrated similar N_2 adsorption behavior when $P/P_0 \leqslant 0.1$. However, TS-1/Dt_{24} exhibited a well-developed hysteresis loop and even higher adsorption amount than TS-1_{24} when $P/P_0 \approx 0.4$ (Fig. 4), which could be due to the mitigated agglomeration and improved dispersity of TS-1 nanoparticles on the surface of the diatomite.

The dramatic micropore population centered at approximately 0.6 nm found in all samples, as shown in Fig. 5a, is ascribed to the inherent micropores of the TS-1 nanoparticles. The mesopore population centered at 2.4 nm is attributed to smaller stacking voids of the TS-1 nanoparticles. Additionally, two mesopore populations, centered at 12.7 and 17.1 nm, are attributed to larger stacking mesopores, consistent with the hysteresis loop in TS-1_{24} and all TS-1/Dt composites (Fig. 4). The observed mesopore distribution range (5–10 nm) and the new population centered at 10.2 nm in TS-1/Dt_{24} suggest a more extensive distribution, which is the result of the improved dispersion of TS-1 nanoparticles onto diatomite.

As detected by mercury intrusion tests, Dt (Fig. 5b) exhibited a distinct macropore population centered at approximately 3.2 μm that is attributed to the stacking voids of the diatom shells.

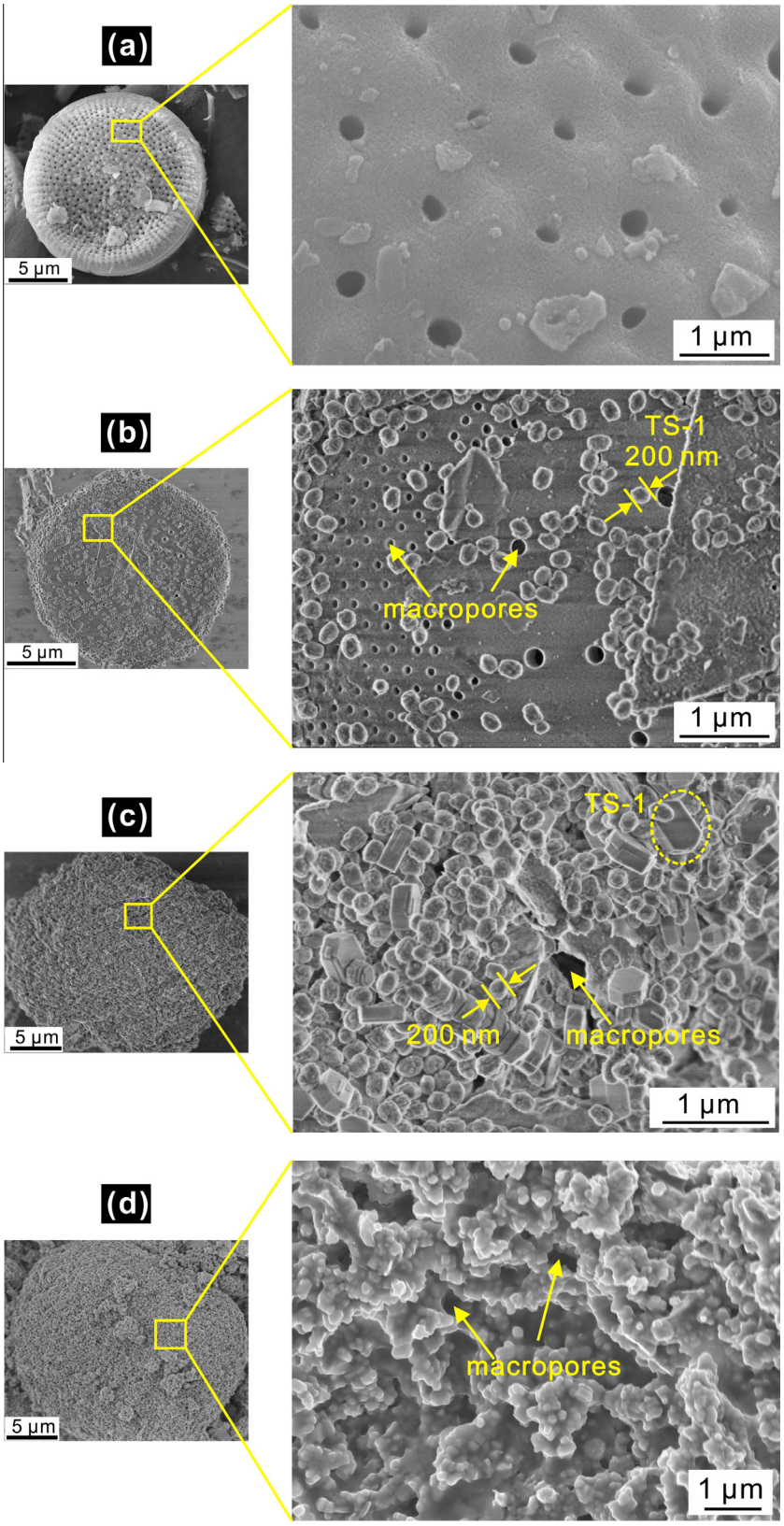

Fig. 2. SEM images of (a) Dt; (b) TS-1/Dt_3; (c) TS-1/Dt_{12} and (d) TS-1/Dt_{24}.

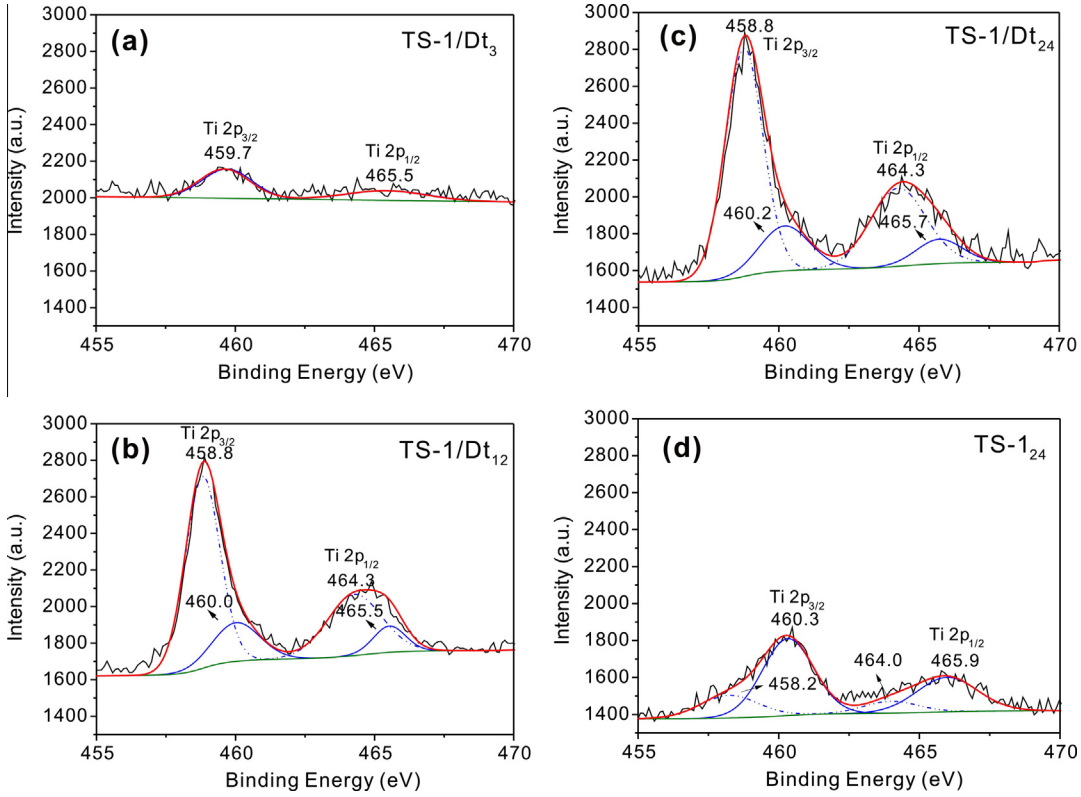

Fig. 3. Deconvolution of the Ti 2p spectrum for (a) TS-1/Dt_3; (b) TS-1/Dt_{12}; (c) TS-1/Dt_{24}; and (d) TS-1_{24}.

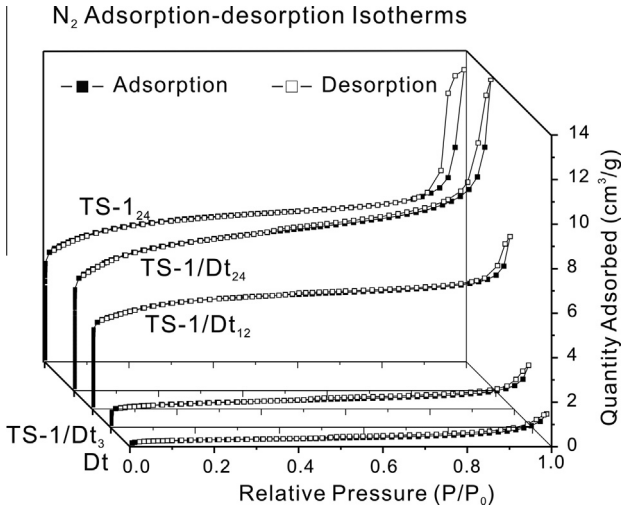

Fig. 4. N_2 adsorption–desorption isotherms of various samples.

Moreover, the two small populations centered at 0.14 and 0.23 μm belong to inherent macropores. In TS-1/Dt_3, the populations were centered at 0.14 and 0.2 μm (Fig. 5b) from the remaining inherent macroporous structure of the diatomite. The 3.9 μm peak, ascribed to stacking voids of the diatom shell, is larger than that in Dt (3.2 μm), due to the coating of TS-1 nanoparticles on the surface of TS-1/Dt_3. The inherent macropores of the diatomite in TS-1/Dt_{12} and TS-1/Dt_{24} were still clearly visible after long hydrothermal time. By contrast, the widening populations centered at 0.14 μm and 0.23 μm were probably due to partial obstruction of the macropores in the diatomite or the dissolution of silicon [53,54] when exposed to the strong alkali TS-1 precursor solution over long hydrothermal treatment time. In addition, unlike those of TS-1/Dt_3, some mesopores (0.03 μm), ascribed to the intergranular mesoporous of the TS-1 nanoparticles emerged in TS-1/Dt_{12} and TS-1/Dt_{24} from higher TS-1 loading amount, which would favor the catalytic performance.

The S_{BET} and $V_{micropore}$ values of Dt were 24.0 m^2/g and 0.009 cm^3/g, respectively (Table 1), and $S_{micropore}$ was much lower than $S_{external}$, indicating the existence of only a few micropores in Dt. TS-1/Dt_3 exhibited much higher S_{BET} (87.3 m^2/g) and $V_{micropore}$ (0.043 cm^3/g) values compared with Dt because of the coating of TS-1 nanoparticles with abundant micropores. TS-1/Dt_{12} showed much higher S_{BET} and $V_{micropore}$ values (388.7 m^2/g and 0.179 cm^3/g, respectively) than the mechanically mixed samples of TS-1 and diatomite (222 m^2/g and 0.0524 cm^3/g, respectively) reported by Liu et al. [42]. These differences were attributed to the diversities in the *in situ* coating mechanism, i.e., PDDA, as a widely used sacrificial charge-modification agent, shows positive when pH value ranges from 0.5 to 14 [55,56]. The surface of PDDA-modified diatomite possessed positive charges, as reported in the previous research [57]. The amorphous SiO_2 and TiO_2 nuclei, produced from the prehydrolysis of the silica and titanium sources were negatively charged. Thus these nuclei were attached electrostatically to the surface of the positively charged modified-diatomite. Eventually, TS-1 nanoparticles were synthesized and evenly dispersed on the surface of a single diatom shell through the hydrothermal growth of the nuclei. The zeolite loading amount of TS-1/Dt_{12} reached 69.4% (Table 1). The resulting composites presented higher S_{BET} and $V_{micropore}$ values than the mechanical mixtures of TS-1 and diatomite because of the higher dispersity of TS-1 nanoparticles, which should lead to better catalytic performance. The S_{BET} and $V_{micropore}$ values of TS-1/Dt_{24} reached 521.3 m^2/g and 0.254 cm^3/g, respectively, which were even higher than those of TS-1_{24}, with a zeolite loading as high as 96.8%; this in

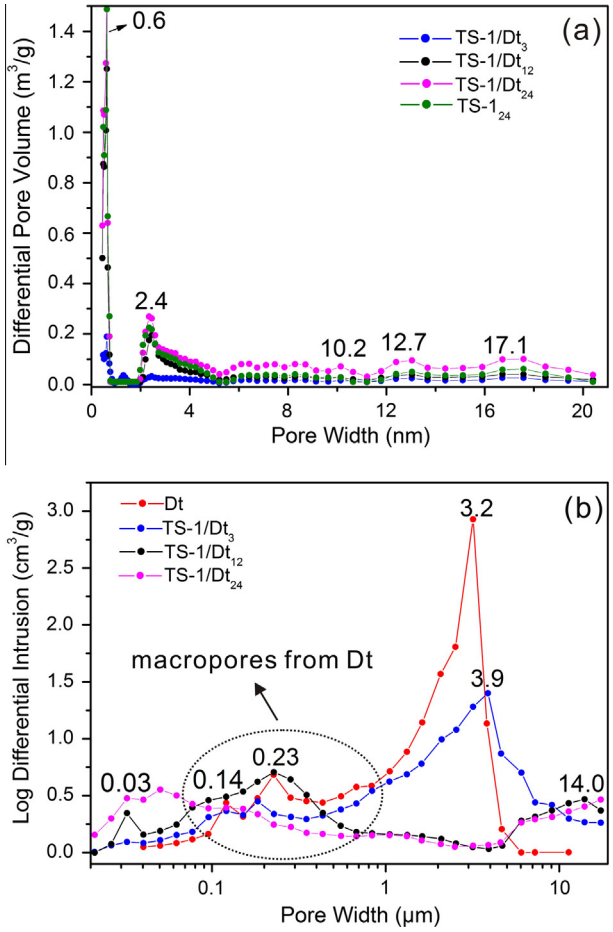

Fig. 5. (a) Micropore and mesopore size distributions (0–20 nm) and (b) Macropore size distributions of TS-1_{24} and TS-1/Dt composites.

turn indicates that the agglomeration of TS-1 nanoparticles was mitigated and their dispersity significantly improved.

3.2. Removal of MB from aqueous solutions by the TS-1/Dt composites

Fig. 6a displays the adsorption curves of MB on various adsorbents as a function of time. The uptake of MB was relatively rapid, and the adsorption on all adsorbents reached equilibrium within 1 h. For Dt, the relative concentration of MB rapidly decreased to steady state after 1 h, with a maximum adsorption efficiency of 73.5%. This result is mainly attributed to the strong electrostatic attraction between Dt and MB molecules and the abundantly macroporous structure of Dt. Initially, MB mainly existed as a cation in the solution at pH = 8 [58], whereas the surface of Dt, composed of amorphous SiO_2 with an isoelectric point of ca. 2.0 [44], was negatively charged. Hence, the positively charged MB molecules aggregated on the surface of the negatively charged Dt via electrostatic attraction, which contributed to the observed adsorption behavior of Dt. Furthermore, the abundant pores of Dt, with a macropore size of 100–800 nm (Fig. 5b), enabled the entry of MB with dimensions of $17.0 \times 7.6 \times 3.25$ Å^3, facilitating increased adsorption. In the case of TS-1/Dt_3, the considerably weak adsorption of MB with an efficiency of 35.5% is attributed to the obstruction of the active adsorption sites on Dt by TS-1 nanoparticles with a higher isoelectric point [45] and the partial blockage of the macropores. TS-1/Dt_{12} and TS-1/Dt_{24} demonstrated much higher MB adsorption efficiencies than TS-1/Dt_3, with values of 50.6% and 70.6%, respectively, owing to their more widely distributed mesopores (Fig. 5a) formed by nanoparticle stacking and higher $S_{external}$ (Table 2). In particular, the calculated maximum adsorption by TS-1/Dt_{24} was 20.23 mg/g, according to the adsorption efficiency in Fig. 6a. This value is close to that of Dt (21.06 mg/g) and exceeds that of pure TS-1_{24} (11.23 mg/g, calculated from Fig. 6a), natural zeolite (14.39 mg/g) [59], ZSM-5 (6.08 mg/g) [60] and modified ZSM-5 (12.41 mg/g) [61], highlighting the significant MB adsorption properties of the novelly synthesized composites.

Under UV-irradiation (Fig. 6b), MB removal by Dt reached equilibrium within 1 h with an efficiency of 74.0%, which was very close to the maximum MB adsorption efficiency (73.5%), indicating none of catalytic activity existed in Dt. Unlike Dt, the relative concentration of MB on TS-1/Dt_{24} decreased substantially, and the removal efficiency reached 90.0% within 1 h, exceeding the adsorption efficiency (70.6%, Fig. 6a) and demonstrating the advantageous synergy of adsorption and photocatalysis on the composites. After 2 h, the MB removal efficiency reached 99.1%. This value is slightly higher than that of pure TS-1_{24} (Fig. 6b), which is likely because of the synergistic removal mechanism of the composites. That is, the newly formed hierarchically porous structure provided easier access for MB molecules, which partly contributes to their removal from aqueous solution. Subsequently, the MB molecules taken up by the composites were further oxidized and decolored by photo-generated hole and electron pairs in the Ti of TS-1, produced by UV excitation. The order of maximum MB removal amount by the TS-1/Dt composites was TS-1/Dt_3 (14.42 mg/g) <TS-1/Dt_{12} (22.45 mg/g) <TS-1/Dt_{24} (28.40 mg/g), calculated based on the removal efficiency and in good agreement with the progression of zeolite loading shown in Fig. 2 and Table 1. In comparison, the removal amount by TS-1/Dt_{24} was almost three times higher than that of the conventional photocatalyst, TiO_2 (12.56 mg/g) [62], and much higher than that of the TiO_2/diatomite composites (19.6 mg/g) [63]. This further underscores the excellent MB removal properties of the novelly synthesized composites via the combination of adsorption and photocatalysis.

The kinetic curves of the MB adsorption and UV-driven removal on TS-1_{24} and TS-1/Dt_{24} were simulated using the pseudo-first-order Lagergren equation [59] respectively with the rate expression given below:

$$q_t/q_{e(0)} = 1 - \exp(-kt) \quad (1)$$

Table 1
N_2 adsorption–desorption results for various samples.

Sample	S_{BET} ($m^2\ g^{-1}$)	$S_{micropore}$[a] ($m^2\ g^{-1}$)	$S_{external}$[a] ($m^2\ g^{-1}$)	V_{total} ($cm^3\ g^{-1}$)	$V_{micropore}$[b] ($cm^3\ g^{-1}$)	$W_{zeolite}$[c] (%)
Dt	24.5	4.3	20.2	0.051	0.009	–
TS-1/Dt_3	87.3	49.2	38.1	0.096	0.043	–
TS-1/Dt_{12}	388.7	210.1	178.6	0.269	0.179	69.4
TS-1/Dt_{24}	521.2	326.9	194.3	0.485	0.254	96.8
TS-1_{12}	508.7	345.5	163.2	0.430	0.245	100
TS-1_{24}	497.4	346.9	150.5	0.455	0.253	100

$W_{zeolite}$% = [$V_{micropore}$ (TS-1/Dt composites) − $V_{micropore}$ (Dt)] × 100%/$V_{micropore}$ (pure TS-1 nanoparticles).
[a] $S_{micropore}$ was calculated from the *t*-plot surface area, and $S_{external} = S_{BET} - S_{micropore}$.
[b] The micropore volume $V_{micropore}$ was determined using the HK method.
[c] The wt.% of zeolite in TS-1/Dt_{12} and TS-1/Dt_{24} were calculated from the micropore volumes using the equation.

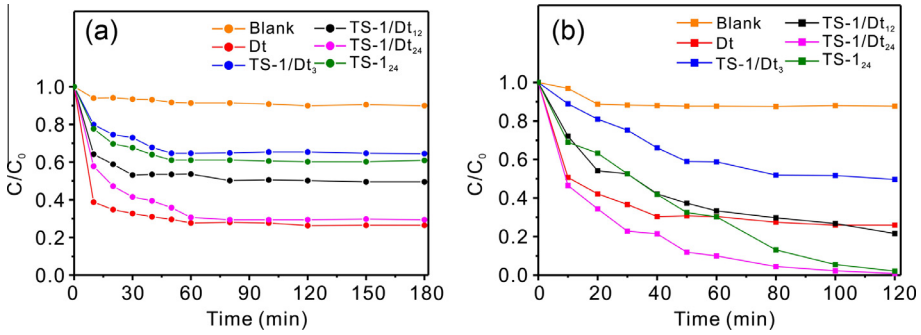

Fig. 6. (a) Adsorption and (b) UV-driven removal of MB using various samples.

Table 2
Parameters of the kinetic models for MB removal on TS-1_{24} and TS-1/Dt_{24}.

Samples	MB adsorption process				MB removal process			
	k (min^{-1})	q_e (mg/g)	R^2	$t_{1/2}$ (min)	k (min^{-1})	q_0 (mg/g)	R^2	$t_{1/2}$ (min)
TS-1_{24}	7.00×10^{-2}	11.4	0.989	9.90	2.43×10^{-2}	28.1	0.976	28.5
TS-1/Dt_{24}	6.95×10^{-2}	20.2	0.976	9.97	5.28×10^{-2}	28.4	0.970	13.1

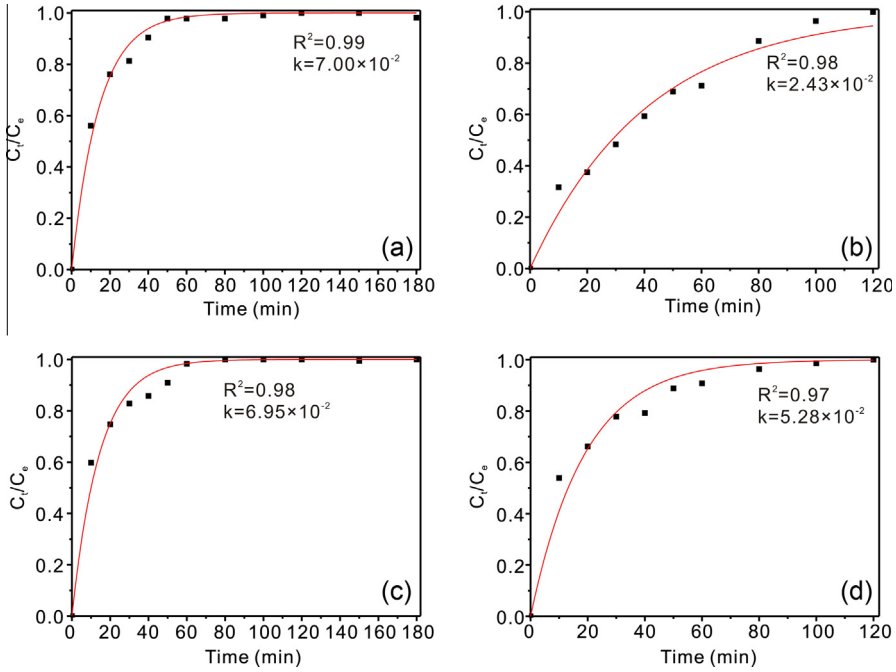

Fig. 7. Simulated kinetics of MB adsorption and UV-driven removal (a), (b) on TS-1_{24} and (c), (d) on TS-1/Dt_{24}, respectively.

where k is the first-order rate constant (min^{-1}), and q_t and q_e are the amounts of MB taken up by each sample per unit mass (mg/g) at any time t and at equilibrium (or q_0, the total removal amount within 2 h for UV-driven removal process), respectively.

As shown in Fig. 7, the adsorptions by TS-1_{24} (Fig. 7a) and TS-1/Dt_{24} (Fig. 7c) were well-fitted by Eq. (1) ($R^2 > 0.97$), indicating that physical diffusion, rapid external surface diffusion, and subsequent MB diffusion into the pores and capillaries of the composites played a dominant role during adsorption [64]. The UV-driven processes on TS-1/Dt_{24} (Fig. 7b) and TS-1_{24} (Fig. 7d) were also represented well as pseudo-first-order reactions ($R^2 > 0.97$), and the MB removal parameters are listed in Table 2. TS-1/Dt_{24} and TS-1_{24} showed similar apparent MB adsorption rates (Table 2), whereas the removal rate constant of MB on TS-1/Dt_{24} (5.28×10^{-2} min^{-1}) was more than twice as high as that on TS-1_{24} (2.43×10^{-2} min^{-1}), with a much shorter half-life (13.1 min). These findings indicate the superior photocatalytic performance of TS-1/Dt_{24} for the removal of MB. This could be due to the greater attachment of MB molecules to the surface of TS-1/Dt_{24} because of this material's improved adsorption properties, which greatly decreased the contact distance and time between guest molecules and the composites and in turn promoted rapid diffusion and the progression of the photocatalytic reaction.

4. Conclusions

In this study, a novel hierarchically porous TS-1/Dt composite was prepared via a facile surface modification, followed by the

hydrothermal synthesis route for the removal of dyes. TS-1 nanoparticles were coated *in situ* on the surface of a single diatom shell. The resulting TS-1/Dt composites possessed much higher specific area and micropore volume than the mechanical mixing samples of TS-1 and diatomite [32,41–43], and also exhibited superior removal efficiency for MB (99.1% after 2 h) compared to pure TS-1 nanoparticles, and the conventional TiO_2 [62] and TiO_2/diatomite photocatalyst [63], as simulated using a pseudo-first-order model. The outstanding dye removal performance of the TS-1/Dt composites was ascribed to their improved adsorption properties, which worked in conjunction with the subsequent UV-photocatalyzed reaction. The agglomeration of TS-1 nanoparticles was alleviated with a maximum zeolite loading of 96.8%, and hierarchically porous structures were formed, which provided more accessible entryways for the uptake of MB. This improved the contact between catalysts and dyes and enhanced the photocatalytic performance. With such remarkable MB removal performance, this novel hierarchically porous TS-1/Dt composite is a promising candidate for adsorption and catalysis of macromolecule organic compounds in waste water.

It is noteworthy that the novelly in-situ synthesized TS-1/Dt composites through a facile surface modification exhibited more excellent removal property for macromolecular organic compounds in water disposal than pure TS-1 and TiO_2 photocatalysts. Whether can the composites show superior removal performance for macromolecular gaseous organic contaminants than pure TS-1 and TiO_2, replacing the conventional photocatalyst with such a low Ti content? Now we are focusing on it.

Acknowledgments

This work was supported by the Team Project of the Natural Science Foundation of Guangdong Province, China (Grant No. S2013030014241), the National Key Technology Research and Development Program of the Ministry of Science and Technology of China (Grant No. 2013BAC01B02), the Natural Science Foundation of China (Grant No. 41202024), and the Science and Technology Program of Guangzhou (Grant No. 201510010138), China. This is a contribution (No. IS-2142) from GIGCAS.

Appendix A. Supplementary material

Supplementary data associated with this article can be found, in the online version, at http://dx.doi.org/10.1016/j.jcis.2015.09.067.

References

[1] V. Gupta, B. Gupta, A. Rastogi, S. Agarwal, A. Nayak, J. Hazard. Mater. 186 (2011) 891–901.
[2] T. Robinson, G. McMullan, R. Marchant, P. Nigam, Bioresour. Technol. 77 (2001) 247–255.
[3] Y. Yu, Y.Y. Zhuang, Z.H. Wang, J. Colloid Interface Sci. 242 (2001) 288–293.
[4] G. Dotto, L. Pinto, J. Hazard. Mater. 187 (2011) 164–170.
[5] S. Allen, G. Mckay, J. Porter, J. Colloid Interface Sci. 280 (2004) 322–333.
[6] Y. He, G. Li, H. Wang, J. Zhao, H. Su, Q. Huang, J. Membr. Sci. 321 (2008) 183–189.
[7] C.A. Martínez-Huitle, E. Brillas, Appl. Catal. B: Environ. 87 (2009) 105–145.
[8] S.H.S. Chan, T. Yeong Wu, J.C. Juan, C.Y. Teh, J. Chem. Technol. Biotechnol. 86 (2011) 1130–1158.
[9] S. Kansal, M. Singh, D. Sud, J. Hazard. Mater. 141 (2007) 581–590.
[10] K. Rajeshwar, M. Osugi, W. Chanmanee, C. Chenthamarakshan, M.V.B. Zanoni, P. Kajitvichyanukul, R. Krishnan-Ayer, J. Photochem. Photobiol. C: Photochem. Rev. 9 (2008) 171–192.
[11] M. Rauf, S.S. Ashraf, Chem. Eng. J. 151 (2009) 10–18.
[12] G.D. Lee, S.K. Jung, Y.J. Jeong, J.H. Park, K.T. Lim, B.H. Ahn, S.S. Hong, Appl. Catal. A:Gen. 239 (2003) 197–208.
[13] H.L. Hsu, R. Selvin, L.S. Roselin, P. Kumari, J.W. Cao, React. Kinet. Catal. Lett. 98 (2009) 265–272.
[14] Z. Juan, Z. Dishun, Y. Liyan, L. Yongbo, Chem. Eng. J. 156 (2010) 528–531.
[15] M. Taramasso, G. Perego, B. Natori, U.S. Patent, NO. 4410501, 1983.
[16] T. Ban, S. Kondoh, Y. Ohya, Y. Takahashi, Phys. Chem. Chem. Phys. 1 (1999) 5745–5752.
[17] H. Yamashita, S. Kawasaki, Y. Ichihashi, M. Harada, M. Takeuchi, M. Anpo, G. Stewart, M.A. Fox, C. Louis, M. Che, J. Phys. Chem. B 102 (1998) 5870–5875.
[18] X. Zhang, Z. Jin, Y. Li, S. Li, G. Lu, Appl. Surf. Sci. 254 (2008) 4452–4456.
[19] P. Yuan, M. Fan, D. Yang, H. He, D. Liu, A. Yuan, J. Zhu, T. Chen, J. Hazard. Mater. 166 (2009) 821–829.
[20] P. Yuan, D. Liu, M. Fan, D. Yang, R. Zhu, F. Ge, J. Zhu, H. He, J. Hazard. Mater. 173 (2010) 614–621.
[21] K.T. Jung, Y.G. Shul, Chem. Mater. 9 (1997) 420–422.
[22] Y. Lee, W. Ryu, S.S. Kim, Y. Shul, J.H. Je, G. Cho, Langmuir 21 (2005) 5651–5654.
[23] S. Wu, C. Bouchard, S. Kaliaguine, Res. Chem. Intermed. 24 (1998) 273–289.
[24] S. Wu, J.E. Gallot, M. Bousmina, C. Bouchard, S. Kaliaguine, Catal. Today 56 (2000) 113–129.
[25] U. Wilkenhöner, G. Langhendries, F. van Laar, G.V. Baron, D.W. Gammon, P.A. Jacobs, E. van Steen, J. Catal. 203 (2001) 201–212.
[26] A. Corma, M. Navarro, J.P. Pariente, J. Chem. Soc., Chem. Commun. (1994) 147–148.
[27] R. Murugavel, H.W. Roesky, Angew. Chem. Int. Ed. Engl. 36 (1997) 477–479.
[28] L.T.Y. Au, J.L.H. Chau, C.T. Ariso, K.L. Yeung, J. Membr. Sci. 183 (2001) 269–291.
[29] X. Wang, B. Zhang, X. Liu, J.Y. Lin, Adv. Mater. 18 (2006) 3261–3265.
[30] X. Wang, B. Meng, X. Zhang, X. Tan, S. Liu, Chem. Eng. J. 255 (2014) 344–355.
[31] Z. Cherkezova-Zheleva, M. Shopska, I. Mitov, G. Kadinov, Hyperfine Interact. 198 (2010) 195–210.
[32] X. Liu, C. Yang, Y. Wang, Y. Guo, Y. Guo, G. Lu, Chem. Eng. J. 243 (2014) 192–196.
[33] S. Guo, L. Shi, Catal. Today 212 (2013) 137–141.
[34] Y. Wang, Y. Tang, X. Wang, A. Dong, W. Shan, Z. Gao, Chem. Lett. 30 (2001) 1118–1119.
[35] Y. Wang, Y. Tang, A. Dong, X. Wang, N. Ren, Z. Gao, J. Mater. Chem. 12 (2002) 1812–1818.
[36] J. Lu, F. Xu, W. Cai, Microporous Mesoporous Mater. 108 (2008) 50–55.
[37] W. Yu, P. Yuan, D. Liu, L. Deng, W. Yuan, B. Tao, H. Cheng, F. Chen, J. Hazard. Mater. 285 (2015) 173–181.
[38] D. Liu, P. Yuan, D. Tan, H. Liu, M. Fan, A. Yuan, J. Zhu, H. He, Langmuir 26 (2010) 18624–18627.
[39] P. Yuan, D. Liu, D.Y. Tan, K.K. Liu, H.G. Yu, Y.H. Zhong, A.H. Yuan, W.B. Yu, H.P. He, Microporous Mesoporous Mater. 170 (2013) 9–19.
[40] W. Yu, L. Deng, P. Yuan, D. Liu, W. Yuan, F. Chen, Chem. Eng. J. 270 (2015) 450–458.
[41] H. Liu, G. Lu, Y. Guo, Y. Guo, J. Wang, Catal. Today 93 (2004) 353–357.
[42] H. Liu, G. Lu, Y. Guo, Y. Guo, J. Wang, Chem. Eng. J. 108 (2005) 187–192.
[43] H. Liu, G. Lu, Y. Guo, Y. Guo, J. Wang, Chem. Eng. J. 116 (2006) 179–186.
[44] Y. Yang, J. Wu, Z. Huang, R. Chen, A. Dai, J. Inorg. Chem.-Nanjing 13 (1997) 11–15.
[45] H. Peng, L. Xu, H. Wu, Z. Wang, Y. Liu, X. Li, M. He, P. Wu, Microporous Mesoporous Mater. 153 (2012) 8–17.
[46] P.T. Hang, G. Brindley, Clays Clay Miner. 18 (1970) 203–212.
[47] W. Zhang, C. Zhou, W. Zhou, A. Lei, Q. Zhang, Q. Wan, B. Zou, Bull. Environ. Contam. Toxicol. 87 (2011) 86–90.
[48] M. Ahmed, E.E. El-Katori, Z.H. Gharni, J. Alloys Compd. 553 (2013) 19–29.
[49] Y. Hasegawa, A. Ayame, Catal. Today 71 (2001) 177–187.
[50] J.S. Reddy, A. Sayari, Stud. Surf. Sci. Catal. 94 (1995) 309–316.
[51] F. Geobaldo, S. Bordiga, A. Zecchina, E. Giamello, G. Leofanti, G. Petrini, Catal. Lett. 16 (1992) 109–115.
[52] A.D. Roddick-Lanzilotta, P.A. Connor, A.J. McQuillan, Langmuir 14 (1998) 6479–6484.
[53] H. Weng, Z. Shen, M. Yuan, D. Guo, J. Chen, Chin. Sci. Bull. 44 (1999) 2205–2208.
[54] P. Miretzky, C. Munoz, E. Cantoral-Uriza, Environ. Chem. Lett. 9 (2011) 55–64.
[55] S. Kidambi, J. Dai, J. Li, M.L. Bruening, J. Am. Chem. Soc. 126 (2004) 2658–2659.
[56] Y.J. Shin, C.C. Su, Y.H. Shen, Mater. Res. Bull. 41 (2006) 1964–1971.
[57] A. Panáček, A. Balzerová, R. Prucek, V. Ranc, R. Večeřová, V. Husičková, J. Pechoušek, J. Filip, R. Zbořil, L. Kvítek, Colloids Surf. B Biointerfaces 110 (2013) 191–198.
[58] C. Tang, J. Zhu, Q. Zhou, J. Wei, R. Zhu, H. He, J. Phys. Chem. C 118 (2014) 26249–26257.
[59] S. Sohrabnezhad, A. Pourahmad, Desalination 256 (2010) 84–89.
[60] X. Jin, M.Q. Jiang, X.Q. Shan, Z.Q. Pei, Z. Chen, J. Colloid Interface Sci. 328 (2008) 243–247.
[61] S. Sohrabnezhad, A. Pourahmad, M.A. Sadjadi, Mater. Lett. 61 (2007) 2311–2314.
[62] B.N. Lee, W.D. Liaw, J.C. Lou, Environ. Eng. Sci. 16 (1999) 165–175.
[63] X.Y. Chuan, X.C. Lu, X.C. Lu, J. Inorg. Mater. 4 (2008) 005.
[64] K. Banerjee, P.N. Cheremisinoff, S.L. Cheng, Water Res. 31 (1997) 249–261.